Supporting Information

Method-dependent Na-ion diffusion in nanocarbon materials: molten-salt-exfoliated graphene and C45 carbon nanoparticles

Yunan Liu, Ali Reza Kamali*

E-mail address: ali@smm.neu.edu.cn; a.r.kamali@cantab.net (A.R. Kamali)

S1. Calculation of the Na^+ diffusion coefficient (D_{Na+}) using cyclic voltammetry (CV)

CV is a widely utilized electrochemical technique for investigating ion-transport kinetics and redox reactions in electrode materials.[1–4] The Na^+ diffusion coefficient (D_{Na^+}) is a crucial kinetic parameter governing charge transport, rate capability, and electrochemical reversibility in Na-ion storage systems. CV was employed to determine the apparent D_{Na^+} based on the Randles–Sevcik (R–S) equation, providing a practical and comparative method for evaluating ion mobility for different electrode materials under consistent experimental conditions.

The R–S equation correlates the peak current (I_p) response with ion diffusion under ideal reversible and diffusion-controlled conditions. The R–S equation was originally developed for reversible redox systems in solution and was later applied for estimating apparent alkali-ion diffusion coefficients in solid-state electrode materials. Its application in Li-ion diffusion became prevalent with the development of intercalation-based Li batteries in the late 20th century and was then extended to Na-ion systems in more recent studies based on Na-ion batteries (SIBs).[5–7] The R–S equation is semiempirical and combines a theoretical solution of Fick's second law of diffusion with experimentally derived constants for reversible electrochemical systems.[8–11] Its application assumes semi-infinite linear diffusion, fast and reversible electron transfer, homogeneous electrode surfaces, and negligible capacitive contributions.[12,13] However, for porous carbon electrodes, these assumptions may not hold completely because the measured I_p can also be influenced by surface-controlled reactions, electric double-layer charging, pseudocapacitive contributions, electrode porosity, and contact resistance. Therefore, the diffusion coefficients obtained using this method should be regarded as apparent diffusion coefficients instead of intrinsic bulk diffusion coefficients. The R–S

method explicitly assumes that the change I_p with scan rate (v) is related to ion diffusion. I_p is expected to show a square-root dependence on v ($I_p \propto v^{\frac{1}{2}}$). However, in porous and nanostructured electrodes, a linear relationship between I_p and v should be interpreted cautiously because similar trends may also originate from mixed kinetic processes involving diffusion and capacitive contributions.[14–16]

$$D_{Na^+} = \left[\frac{I_p}{2.69 \times 10^5 n^{\frac{3}{2}} A v^{\frac{1}{2}} \Delta C_0}\right]^2, \qquad \text{(S1)}$$

where I_p represents the anodic or cathodic peak current, n is the number of electrons transferred, A represents the effective electrode area, $v^{\frac{1}{2}}$ denotes the square root of the scan rate, and ΔC_0 denotes the Na^+ concentration difference. The numerical constant applies at room temperature (298 K). Advantages of this method include its simplicity, low computational demand, and the direct use of experimental CV data without requiring complex modeling or specialized equipment.[17–20] However, the calculated values should be interpreted as apparent kinetic parameters instead of direct measures of intrinsic Na^+ bulk diffusion.[21,22]

Fig. S1(a) shows the CV profiles of the graphene electrode recorded at 0.2, 0.4, 0.6, 0.8, and 1.0 mV s^{-1}, where two characteristic peaks can be observed. Peak 1 corresponds to the cathodic (reduction) process related to Na^+ insertion and exhibits a negative current response. In contrast, Peak 2 represents the anodic (oxidation) process related to Na^+ extraction, yielding a positive current. As v increases, the absolute I_p of both features increases. This trend is consistent with a diffusion-affected electrochemical response, but it should not be regarded as evidence of a purely diffusion-controlled process. At higher scan rates, the time available for ion transport decreases, while surface and near-surface processes may contribute more significantly to the measured current.[23,24]

Fig. S1(b) shows the linear relationship between I_p and $v^{1/2}$ obtained from the R–S analysis for the graphene electrode. Specifically, the peak currents I_p extracted from Fig. S1(a) at each scan rate were plotted as a function of $v^{1/2}$ and fitted linearly. The good linearity of I_p versus

$v^{1/2}$ suggests that the R–S framework can provide a reasonable first-order approximation for comparing apparent Na^+ transport kinetics. However, this linearity alone does not confirm purely diffusion-controlled behavior, especially in porous carbon electrodes, where capacitive and interfacial contributions may co-exist. The slopes of the fitted lines are denoted as b, yielding $b = -15.75$ for Peak 1 and $b = 31.95$ for Peak 2. As the cathodic peak current is negative by convention, $|b|$ was used in subsequent diffusion coefficient calculations.

The same procedure was applied to the C45 electrode, as summarized in Figs. S1(c) and (d), which show CV curves acquired at different scan rates and the corresponding I_p and $v^{1/2}$ linear fits, respectively. Peak 1 and Peak 2 are retained, while the overall I_p magnitude is higher than that of graphene, implying a stronger apparent charge response under identical experimental conditions. This enhancement may originate from several combined factors, including a more effective conductive network, a larger electrochemically active surface area, a porous electrode architecture, and potential pseudocapacitive contributions. Consequently, the diffusion coefficients derived from this approach should be regarded as apparent diffusion coefficients instead of intrinsic bulk values. The fitted slopes obtained from Fig. S1(d) are $b = 32.02$ for Peak 1 and $b = -40.61$ for Peak 2.

Under reversible and diffusion-controlled conditions, the R–S relationship[6] can be expressed as

$$D_{Na^+} = [I_p / (2.69 \times 10^5 \, n^{3/2} \, A \, v^{1/2} \, \Delta C_o)]^2 , \qquad \text{(S2)}$$

where I_p represents the peak current and corresponds to the I_p values of the oxidation and reduction peaks on the CV curve. In addition, n refers to the number of electrons transferred, A represents the effective area of the electrode sheet, $v^{1/2}$ denotes the square root of the scan rate, and ΔC_o represents the concentration difference. Based on the R–S relationship, the apparent D_{Na^+} for the C45 electrode were calculated to be 1.1×10^{-8} and 1.8×10^{-8} cm^2 s^{-1} from the cathodic and anodic peaks, respectively, while graphene exhibited D_{Na^+} values of 2.7×10^{-9} and 1.1×10^{-8} cm^2 s^{-1}. These values provide a useful comparison of apparent Na^+ transport kinetics between C45 and graphene under identical testing conditions. Nevertheless, owing to the porous nature of the electrodes and the possible involvement of surface-controlled and pseudocapacitive processes, these values should be regarded as apparent diffusion coefficients

instead of direct intrinsic bulk diffusion coefficients. Table S1 compares the diffusion coefficients calculated in this study with those reported in other works.

S2. Calculation of D_{Na^+} using the galvanostatic intermittent titration technique (GITT)

The GITT is a widely used electrochemical method for investigating ion transport kinetics in electrode materials and tracking the evolution of quasi-equilibrium potentials.[28–31] D_{Na^+} is an important kinetic parameter that influences charge-transport rates, rate capability, and reaction reversibility in Na-ion storage systems. Unlike continuously perturbed techniques, GITT employs a "short galvanostatic pulse followed by a sufficient relaxation period" protocol, enabling the decoupling of kinetic polarization from thermodynamic potential changes under near-equilibrium condition. This enables a more physically meaningful quantification of Na^+ diffusion behavior at different states of charge (SOC).

In this study, D_{Na^+} was determined using the GITT diffusion coefficient equation, also known as the Weppner–Huggins GITT equation. The GITT method was originally developed by Weppner and Huggins to estimate the chemical diffusion coefficient in solid-state insertion/extraction systems. The central premise of this method is that, under the small concentration perturbation induced by a low-current pulse, ion diffusion within the electrode can be described by Fick's second law, while the transient potential response can be analytically related to time under the semi-infinite diffusion approximation.[32–34] This method has been extensively applied to intercalation electrodes in Li-ion batteries and was later extended to SIB systems to obtain SOC-dependent D_{Na^+} "maps," which can be correlated with thermodynamic features, such as voltage plateaus and phase-transition regions.[35]

The Weppner–Huggins GITT equation is a semi-analytical and semiempirical expression derived from the short-time solution of Fickian diffusion under a constant-flux boundary condition. During the current pulse, the potential variation in the diffusion-controlled regime exhibits a characteristic dependence on $\sqrt{t}$ after the pulse. A sufficiently long relaxation period yields a potential change that more closely approaches quasi-equilibrium. The GITT equation relates the transient potential change during the pulse to the quasi-equilibrium potential change after relaxation and, together with electrode geometric and material parameters (e.g., active mass, molar volume, and effective reaction area), enables quantitative estimation of D_{Na^+}.[36–38]

Accordingly, the key assumptions of this method are that the potential response is governed by solid-state diffusion and that the pulse amplitude is sufficiently small to maintain a linear, small-perturbation regime, such that the potential change reflects intrinsic diffusion kinetics instead of being governed by severe interfacial charge-transfer limitations or side reactions.[39]

GITT offers the following advantages. First, within a near-thermodynamic-equilibrium framework, GITT simultaneously provides quasi-equilibrium voltage profiles and the SOC dependence of the diffusion coefficient, thereby distinguishing thermodynamic processes (e.g., plateaus/phase transitions) from kinetic processes (diffusion rates).[31] Second, GITT does not depend on complex frequency-domain equivalent-circuit fitting or multiparameter inverse modeling; instead, its data-processing workflow is relatively standardized, promoting reproducible comparisons and benchmarking across different material systems.

However, GITT also has nonnegligible limitations. First, the GITT diffusion equation is derived under the assumptions of semi-infinite diffusion, linear response under small perturbations, a uniform effective reaction area, and approximately constant material properties. If pronounced phase transitions, strong polarization, significant side reactions, or charge-transfer processes become rate-limiting, the pulse-induced potential change is no longer diffusion-dominated, and the resulting D_{Na^+} may deviate from the true diffusion coefficient.[40] Moreover, practical electrodes are typically porous composites, where ion transport depends on coupled processes, such as intra-particle diffusion, pore-scale mass transport, interfacial reactions, and solid electrolyte interface (SEI) effects; consequently, GITT generally provides an apparent/effective diffusion coefficient that reflects overall kinetics rather than the intrinsic bulk diffusivity of an ideal single-phase solid.[41,42] Moreover, GITT requires long relaxation times to obtain reliable quasi-equilibrium potential changes, making the measurements time-consuming. Insufficient relaxation can also systematically bias the calculated diffusion coefficients. Finally, the results are sensitive to IR correction, selection of the linear fitting window, pulse current magnitude, and pulse duration, and differences in data-treatment protocols across studies may affect inter-study comparability.

Fig. S2(a) shows the full voltage–time profile obtained from the graphene electrode during GITT measurements conducted at a current density of 30 mA g^{-1} in the first electrochemical cycle. The curve exhibits a characteristic “saw-tooth” pattern, which originates from the

repeated execution of identical GITT titration steps. Each "tooth" represents one complete titration step consisting of a 30 min galvanostatic charge/discharge pulse, during which the cell voltage responds rapidly, typically appearing as a voltage step superimposed on a gradual slope. This is followed by a 90 min open-circuit relaxation period, during which the voltage progressively recovers toward a new quasi-equilibrium steady-state potential (E_s) corresponding to the updated SOC. Consequently, the continuous saw-tooth structure observed in Fig. S2(a) essentially represents a sequential superposition of numerous identical "current pulse + relaxation" units, reflecting the stepwise evolution of the electrode over the entire voltage window.

Fig. S2(b) shows an enlarged view of a representative single saw-tooth unit extracted from Fig. S2(a) and magnified along the time axis to clearly illustrate the key electrochemical parameters used for calculating the D_{Na^+}. As shown in Fig. S2(b), one complete GITT titration step can be divided into several successive stages with distinct physical meanings. Before the galvanostatic pulse is applied, the cell remains under open-circuit conditions and fully relaxes from the previous titration step. The voltage at this stage is relatively stable and can be regarded as the initial quasi-equilibrium potential (E_s) of the current step, representing the thermodynamic state of the electrode at the corresponding SOC. After initiating the galvanostatic pulse, the voltage exhibits an instantaneous vertical jump, explicitly labeled as the IR drop in the figure.[43] This abrupt voltage change arises from the internal ohmic resistance of the cell, including contributions from the electrolyte, electrode matrix, current collectors, and interfacial contact resistances. As this component is unrelated to ion diffusion in the solid phase, it is considered a nondiffusion contribution and must be identified and excluded from the diffusion-related polarization during subsequent analysis. After the IR drop, the voltage does not change abruptly but instead increases gradually and continuously under constant current, producing a sloped voltage profile. This stage corresponds to the galvanostatic pulse duration (τ = 30 min), which is marked by vertical dashed lines in Fig. S2(b). The voltage change during this period, denoted as ΔE_τ, represents the magnitude of the potential variation related to the current pulse (typically after excluding the IR drop). This region reflects the gradual development of Na^+ concentration gradients within the electrode under the applied

current and is therefore closely associated with solid-state diffusion and mass transport limitations.[43]

Once the galvanostatic pulse is terminated, the cell returns to open-circuit conditions, and the voltage gradually relaxes from the polarized state toward thermodynamic equilibrium. Because of the relatively long 90-min relaxation period used in this study, the voltage can approach a new quasi-equilibrium value. The horizontal bracket labeled ΔE_s at the end of the relaxation stage represents the difference between the steady-state potentials before and after the pulse, that is, the change from the initial steady-state potential E_s (before the pulse) to the final steady-state potential after relaxation. ΔE_s thus reflects the quasi-equilibrium thermodynamic potential shift related to the SOC change induced by the applied current pulse.

To further verify the adequacy of the 90-min relaxation period, representative GITT pulses from both C45 and graphene electrodes were selected and examined in detail, as shown in Fig. S8. Figs. S7(a)–(c) shows the analysis for the C45 electrode, whereas Figs. S7(d)–(f) shows the corresponding analysis for the graphene electrode. Figs. S8(b) and (e) shows enlarged voltage–time profiles that clearly define the analysis windows, where each selected titration step consists of a 30 min galvanostatic current pulse, followed by a 90-min open-circuit relaxation period. The relaxation regions were further fitted using a single-exponential relaxation function[44]:

$$V(t) = V_{eq} + Ae^{-t/\tau} \qquad \text{(S3)}$$

where $V(t)$ refers to the voltage at relaxation time t, V_{eq}represents the extrapolated equilibrium voltage, A is the relaxation amplitude, and τ denotes the characteristic relaxation time constant. As shown in Figs. S7(c) and (f), the fitting results yielded high correlation coefficients, with $R^2 = 0.9939$ for the C45 electrode and $R^2 = 0.9990$ for the graphene electrode. These high R^2 values indicate that the selected relaxation windows exhibit well-defined voltage relaxation behavior. Moreover, the voltage variation at the final stage of the 90-min relaxation period became small for both electrodes, indicating that the voltage response had entered a slow-drift quasi-equilibrium region. Consequently, the marked fitting windows, high fitting quality, and terminal voltage stabilization behavior support that the 90-min relaxation period is sufficient for extracting reliable quasi-equilibrium voltages for GITT analysis.

Based on the parameters extracted from each individual titration step (E_s, IR drop, ΔE_τ, ΔE_s, and τ), the chemical D_{Na^+} in the graphene-based SIB system can be determined. The diffusion process is assumed to obey Fick's second law, and the D_{Na^+} is calculated using the Weppner–Huggins GITT diffusion equation. D_{Na+} was calculated using the following equation[44]:

$$D_{Na+} = \frac{4}{\pi\tau}\left(\frac{m_B V_m}{M_B S}\right)^2\left(\frac{\Delta E_s}{\Delta E_\tau}\right)^2 \quad \text{(S4)}$$

This calculation incorporates several material and geometric parameters, including the active material mass (m_B), molar volume (V_m), molecular weight (M_B), and effective geometric characteristics of the electrode.

The GITT data shown in Figs. S2(c)–(e) were analyzed using the same procedure as described for Figs. S2(a) and (b). By systematically extracting $\Delta E\tau$ and ΔEs for each titration step and substituting them into the Weppner–Huggins equation, the D_{Na^+} under different materials, current densities, and cycle numbers were obtained. At a current density of 30 mA g^{-1}, the C45 electrode exhibits a D_{Na^+} of 7.74×10^{-10} cm^2 s^{-1} during the first-cycle discharge and 1.6×10^{-9} cm^2 s^{-1} during the first-cycle charge. In the second cycle, the corresponding discharge and charge diffusion coefficients increase to 1.3×10^{-9} cm^2 s^{-1} and 1.43×10^{-9} cm^2 s^{-1}, respectively. In comparison, the graphene electrode shows a first-cycle D_{Na^+} of 1.77×10^{-10} cm^2 s^{-1} during discharge and 5.27×10^{-10} cm^2 s^{-1} during charge. In the second cycle, the discharge diffusion coefficient increases to 5.4×10^{-10} cm^2 s^{-1}, while the charge diffusion coefficient increases markedly to 5.10×10^{-9} cm^2 s^{-1}.

At a higher current density of 100 mA g^{-1}, the C45 electrode exhibits first-cycle discharge and charge diffusion coefficients of 2.4×10^{-10} cm^2 s^{-1} and 3.8×10^{-10} cm^2 s^{-1}, respectively. In the second cycle, the discharge and charge diffusion coefficients are 3.8×10^{-10} cm^2 s^{-1} and 3.9×10^{-10} cm^2 s^{-1}, respectively. For the graphene electrode, the first-cycle D_{Na^+} at 100 mA g^{-1} are 9.18×10^{-10} cm^2 s^{-1} during discharge and 3.0×10^{-9} cm^2 s^{-1} during charge. In the second cycle, the discharge diffusion coefficient further increases to 2.02×10^{-9} cm^2 s^{-1}, while the charge diffusion coefficient remains at 3.0×10^{-9} cm^2 s^{-1}.

During a GITT discharge–rest sequence, a small constant current is first applied for a short pulse, followed by an open-circuit relaxation step. The corresponding $V–t^{1/2}$ plot (Fig. S8)

shows the voltage evolution during the current pulse. Immediately following the onset of the pulse, the potential exhibits a rapid increase due to ohmic IR drop and interfacial polarization. After this transient step, the voltage increases continuously with time and presents a noninstantaneous, time-dependent response consistent with diffusion-governed behavior in GITT measurements. Notably, after excluding the initial IR drop, the V–$t^{1/2}$ curve can be divided into two regimes with different apparent slopes: an earlier regime affected by near-surface insertion and interfacial transport, and a later regime characterized by a smaller slope, suggesting that ion transport is increasingly governed by solid-state diffusion within the electrode bulk. This evolution from surface-related kinetics to diffusion-limited transport provides the basis for choosing an appropriate linear fitting window in the V–$t^{1/2}$ representation. The potential change during the pulse, $\Delta E\tau$ (determined from the fitted region), along with the quasi-equilibrium potential shift after the subsequent rest step, ΔEs, is subsequently used to calculate the chemical diffusion coefficient and assess the ion-transport kinetics of the anode material.[45,46]

Notably, if the relaxation time was insufficient, the equilibrium voltage shift ΔEs would be underestimated, leading to an underestimation of the calculated diffusion coefficient. Since a relatively long relaxation time was used in this work, the effect of incomplete relaxation is minimized. These explanations and the representative V–$t^{1/2}$ plot have been added to the revised manuscript to clarify the fitting procedure and demonstrate the validity of the GITT-derived diffusion coefficient.

Table S2 compares the diffusion coefficients obtained in this study with those obtained from previous studies.

S3. Calculation of D_{Na^+} using electrochemical impedance spectroscopy (EIS)

EIS is a powerful and widely used electrochemical characterization technique for investigating charge transport, interfacial kinetics, and mass transfer processes in electrode materials over a broad frequency range.[50–52] EIS involves applying a small-amplitude sinusoidal voltage or current perturbation to an electrochemical system under near-steady-state conditions and analyzing the resulting impedance response as a function of frequency. This frequency-dependent response allows the deconvolution of distinct physicochemical processes based on their characteristic time constants. These processes typically include ohmic resistance

arising from the electrolyte and current collectors, charge-transfer reactions at the electrode–electrolyte interface, electric double-layer polarization, and ion diffusion within the bulk electrode material. EIS has been extensively used in SIB systems to investigate Na^+ transport both within the solid electrode phase and across the electrode–electrolyte interface. Consequently, EIS has emerged as an effective and widely adopted method for estimating the apparent D_{Na^+} in Na-ion storage materials.[53–56]

The determination of D_{Na^+} based on EIS mainly depends on analyzing the low-frequency region of the impedance spectrum. In this frequency domain, mass transport progressively dominates the overall electrochemical kinetics. Upon application of a small alternating perturbation, Na^+ migration within the electrode is required to compensate for perturbation-induced concentration gradients, causing ion diffusion to have a pronounced effect on the impedance response. Therefore, the low-frequency region of the Nyquist plot typically exhibits a linear tail with an inclination close to 45°, which is characteristic of diffusion-controlled behavior and is commonly referred to as the Warburg impedance. This feature corresponds to the semi-infinite linear diffusion of Na^+ within the solid electrode under small-signal conditions, which can be rigorously described using Fick's second law of diffusion formulated in the frequency domain.[57–60]

The theoretical origin of diffusion-related impedance can be traced back to classical electrochemical studies on diffusion-limited reactions at planar electrodes. In liquid electrolyte systems, diffusion introduces a frequency-dependent impedance component that regulates electrode kinetics at low frequencies. Following the emergence and rapid development of intercalation-type battery electrodes in the late 20th century, this theoretical framework was adapted to describe ion transport within solid electrode materials. This advancement allowed impedance spectroscopy to be used as a powerful tool for investigating solid-state ion diffusion processes.[61] In the rapidly evolving field of SIBs, EIS-based diffusion analysis has been widely used to evaluate the apparent D_{Na^+} of diverse electrode materials, such as carbonaceous electrodes and inorganic intercalation compounds.[62]

Assuming semi-infinite diffusion, the real part of the impedance in the low-frequency region varies linearly with the inverse square root of the angular frequency. By appropriately fitting this linear regime, a diffusion-related characteristic parameter, commonly referred to as

the Warburg coefficient, can be extracted. When combined with fundamental physical constants, electrode geometry, and the effective Na^+ concentration in the active material, this parameter allows quantitative evaluation of Na^+ transport kinetics and subsequent determination of the D_{Na^+}. In this way, EIS establishes a direct and physically meaningful link between the experimentally measured impedance response and ion transport dynamics within the electrode.[63] The EIS-based determination of D_{Na^+} provides several distinct advantages. Because of the use of small-amplitude perturbations and measurements performed under near-equilibrium conditions, this method enables ion diffusion to be analyzed without inducing considerable polarization or structural perturbations in the electrode. Moreover, the frequency-domain nature of EIS provides access to the characteristic time and length scales related to solid-state ion transport, such that the obtained diffusion coefficient reflects the dynamic response of Na^+ to concentration gradients within the electrode matrix.[64]

However, it should be emphasized that D_{Na^+} derived from EIS are generally apparent or effective values, instead of intrinsic lattice diffusion parameters. This distinction occurs because the diffusion-related impedance response typically includes the coupled contributions of bulk diffusion, grain-boundary transport, ion migration within pores, and interfacial phenomena such as surface films or SEI layers. In addition, the reliability of the extracted diffusion coefficients critically depends on the validity of the semi-infinite diffusion assumption and the quality of the low-frequency impedance data. Deviations from ideal diffusion behavior, such as finite-length diffusion, nonuniform current distribution, or pronounced pseudocapacitive effects, may introduce uncertainties and bias in the determination of diffusion parameters.

Fig. S3 presents the EIS spectra of graphene and C45 electrodes in fresh cells and after 150 charge–discharge cycles, underscoring the evolution of ion transport kinetics during cycling. As shown in the Nyquist plots in Figs. S3(a) and (c), both electrodes exhibit a typical impedance response comprising a high-frequency intercept attributed to ohmic resistance, a depressed semicircle in the medium-frequency region corresponding to charge-transfer processes, and a low-frequency sloping tail indicative of diffusion-controlled Na^+ transport. Notably, the low-frequency Warburg tail becomes remarkably less steep for the graphene electrode after prolonged cycling, suggesting a substantial decrease in diffusion impedance,

whereas the C45 electrode exhibits a more moderate change. For quantitative evaluation of Na^+ diffusion kinetics, the real part of the impedance (Z') in the low-frequency region was plotted as a function of $\omega^{-1/2}$ (Figs. S3(b) and (d)), where a linear relationship was observed under the assumption of semi-infinite diffusion. The slopes of these linear fits correspond to the Warburg coefficients (σ), which decrease from 68.91 to 1.68 for graphene and from 70.59 to 21.1 for C45 after 150 cycles. Based on these σ values, the apparent D_{Na^+} were calculated. Furthermore, the ion diffusion coefficient (D) was determined by fitting the Warburg region in the low-frequency domain using the established theoretical equations provided below[64]:

$$\omega = 2\pi f \quad \text{(S5)}$$

$$Z_w = R + \sigma\omega^{-1/2} \quad \text{(S6)}$$

$$D = 0.5R^2T^2/S^2n^4F^4C^2\sigma^2 \quad \text{(S7)}$$

The values of the diffusion coefficients were calculated to be 4.99×10^{-14} and 8.4×10^{-11} $cm^2\ s^{-1}$ for fresh and cycled graphene electrodes, and 4.75×10^{-14} and 5.3×10^{-13} $cm^2\ s^{-1}$ for fresh and cycled C45 electrodes. The significant enhancement in Na^+ diffusion for graphene upon cycling reflects a substantial alleviation of diffusion resistance. Conversely, the more moderate improvement observed for C45 suggests comparatively stable but less dramatically enhanced ion transport. Overall, these findings show that cycling induces distinct interfacial and bulk transport evolution in different carbon electrodes, as effectively captured by EIS-based diffusion analysis. Table S3 compares the diffusion coefficient calculated in this study with those obtained in previous works.

S4. Preparation of graphene using the molten salt exfoliation method

High-purity industrial artificial graphite rods (purity >99%, diameter 13 mm, and length 300 mm) were purchased from Goodfellow (UK) and used as the precursors for preparing graphene nanosheets. Graphene was synthesized via an electrochemical exfoliation method conducted in a molten salt medium; Fig. S4 illustrates the experimental configuration and procedure. The electrochemical process was performed in a vertically oriented tubular Inconel alloy reactor placed inside a resistance furnace, ensuring both mechanical robustness and chemical inertness under high-temperature conditions. The reactor was sealed at the top using

a steel lid, along with O-ring gaskets and mechanical compression fixtures, to maintain an airtight environment and prevent air ingress. The molten salt electrolyte comprised sodium chloride (Sigma Aldrich S9888, 800 g) and lithium chloride (400 g), which were thoroughly mixed and loaded into a graphite crucible with an inner diameter of 10 cm and a height of 20 mm. The graphite crucible simultaneously functioned as the anode during electrolysis. The artificial graphite rod was vertically immersed in the molten salt and connected to an external DC power supply, thereby forming a complete electrochemical circuit. All experiments were performed under a flowing Ar–4% H_2 protective atmosphere at a constant flow rate of 200 cm^3 min^{-1}. The furnace temperature was increased to 820 °C at a controlled heating rate of 5 °C min^{-1}. Under these conditions, the salt mixture became fully molten, and the actual melt temperature was continuously monitored using a thermocouple immersed directly in the molten salt, yielding a stable temperature of approximately 780 °C (Fig. S4). Next, a constant direct current of 40 A was applied between the anode and cathode for 80 min to initiate and sustain the electrochemical exfoliation of the graphite cathode. Throughout the electrolysis process, the potential difference between the electrodes was monitored using a quasi-reference electrode. This electrode consisted of a Mo wire partially encased in an alumina tube and immersed in the molten salt (denoted as R_E in Fig. S4), ensuring reliable electrochemical measurements under harsh high-temperature conditions. After completion of electrolysis, the system was allowed to cool naturally to room temperature under a protective atmosphere. The solidified salt was then removed by repeated washing with deionized water, followed by vacuum filtration to collect the exfoliated carbon material from the graphite cathode. The product thus obtained appeared as a black, lightweight, and loosely aggregated powder, which was referred to as graphene nanosheets in this study. More details on electrolysis can be found in [68].

S5. Preparation and assembly of batteries

Electrochemical performance was assessed using CR2032-type coin half cells. In these cells, carbon-based materials were used directly as the active components of the working electrode, and no additional conductive additives were introduced. Na metal served as the counter/reference electrode, while a glass fiber separator (Whatman, GF/A) was used to

electrically isolate the electrodes. The working electrodes were prepared by mixing the carbon material with a polyvinylidene fluoride (PVDF) binder at a weight ratio of 9:1. PVDF was first dissolved in *N*-methyl-2-pyrrolidone, followed by the gradual addition of the nanocarbon material. The obtained mixture was stirred continuously for 12 h to ensure sufficient dispersion and slurry homogeneity. Subsequently, the slurry was cast onto copper foil current collectors and dried overnight under vacuum at 100 °C, resulting in an areal loading of active material in the range of 1.0–1.2 mg cm^{-2}.

A diglyme-based electrolyte comprising 1.0 M sodium trifluoromethanesulfonate ($NaCF_3SO_3$) dissolved in pure diglyme (100 vol%) was used. Cell assembly was performed entirely in an argon-filled glovebox, where H_2O and O_2 concentrations were strictly maintained below 0.01 ppm. Galvanostatic charge–discharge tests were performed at 25 °C within a voltage window of 0.01–2.5 V using a LAND battery testing system. CV and EIS were performed using a CHI 660E electrochemical workstation. For EIS, a small-amplitude sinusoidal voltage perturbation of 5 mV was applied under steady-state conditions over a frequency range of 100 kHz to 10 mHz.

Supplementary Figures

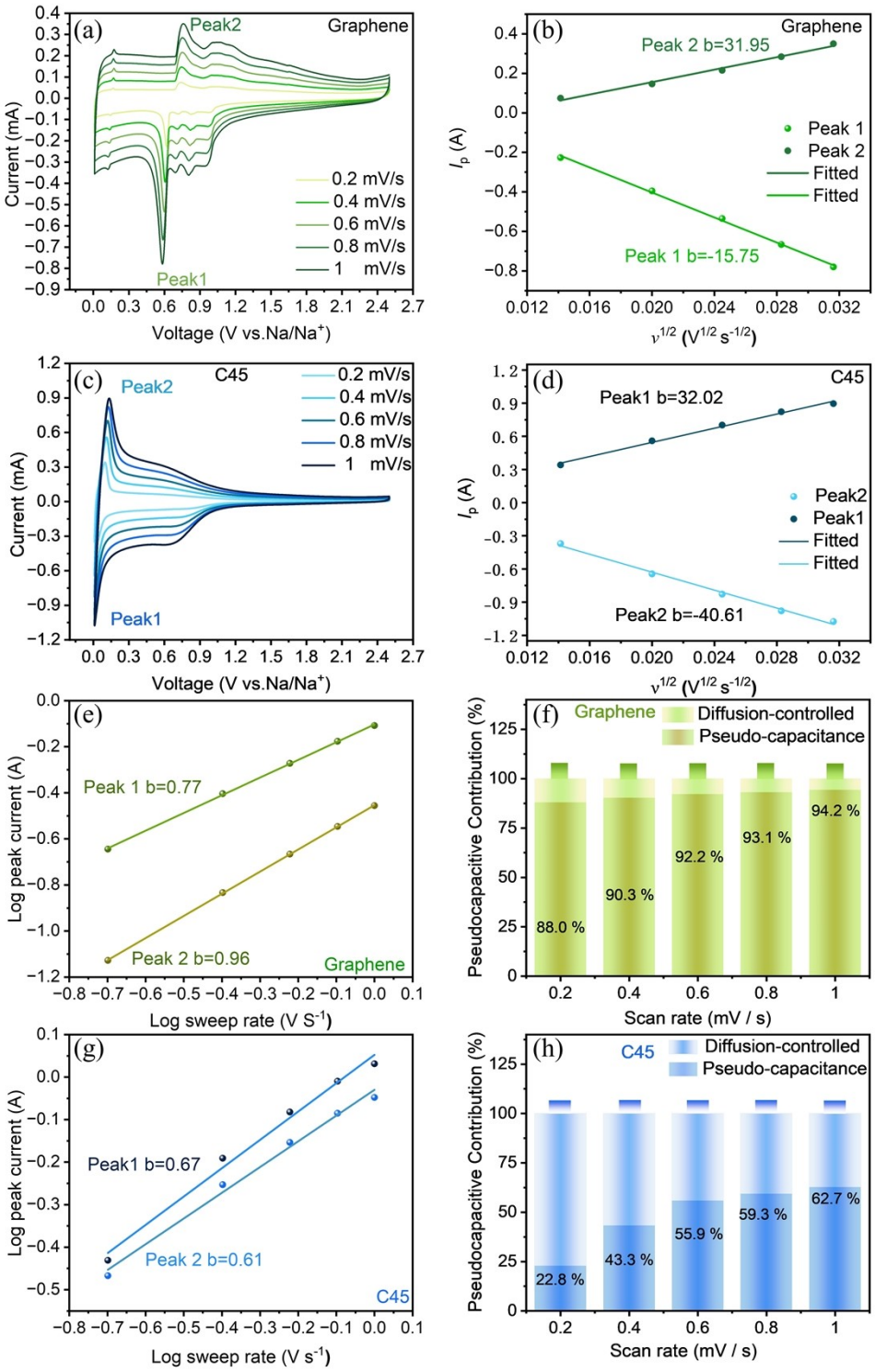

Fig. S1. (a,c) Cyclic voltammetry (CV) curves at scan rates (υ) of 0.2−1.0 mV s^{-1} for graphene and C45. (b,d) Linear relation between peak current (I_p) and the square root of scan rate ($v^{1/2}$) for graphene and C45. Linear fitting of log (υ) vs log (I_p) for (e) graphene and (g) C45. Contribution of various mechanisms to the Na-ion storage performance of (f) graphene and (h) C45.

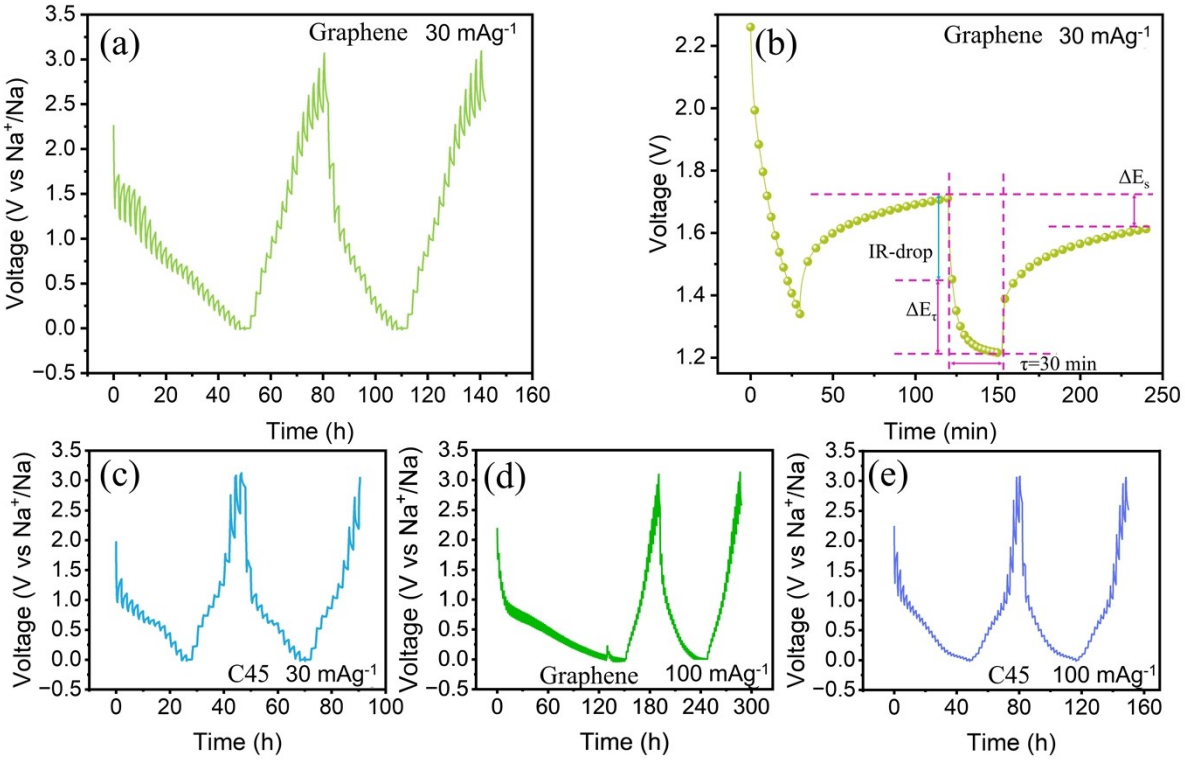

Fig. S2. (a) Galvanostatic intermittent titration technique (GITT) profiles of graphene at 30 mA g^{-1}. (b) Demonstration of a single titration at 2.3 V during the GITT measurement of the graphene electrode. (c–e) GITT profiles of C45 and graphene electrodes at 30 and 100 mA g^{-1}.

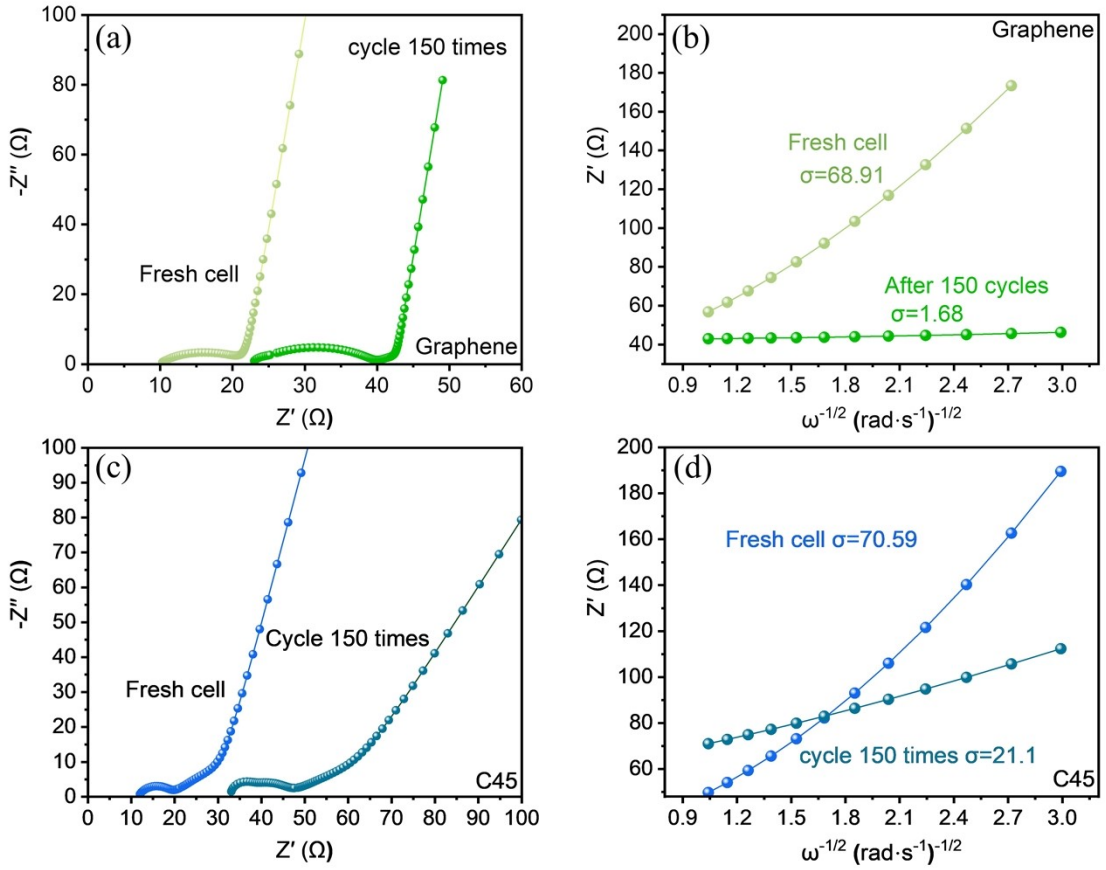

Fig. S3. Nyquist curves of cells in ether-based electrolytes: (a,c) Fresh and cycled C45- and graphene-based electrodes. (b,d) Plots of $\omega^{-1/2}$ versus Z' for fresh and cycled electrodes.

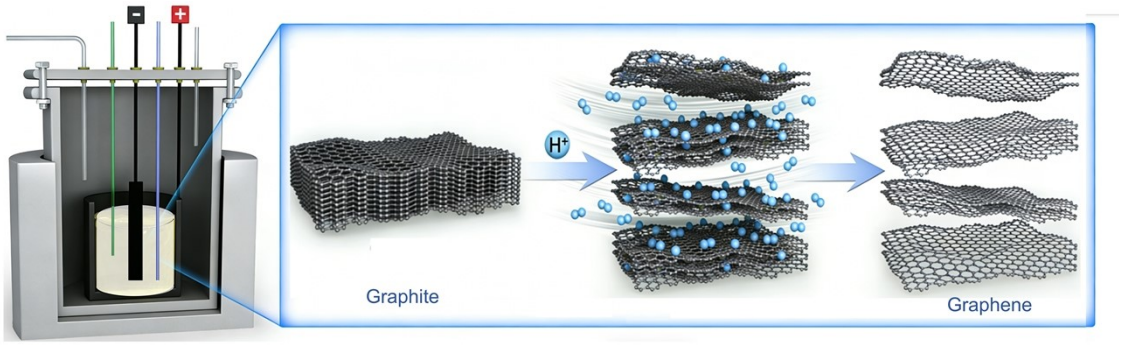

Fig. S4. Schematic representation of the molten salt exfoliation method used to prepare graphene nanosheets.

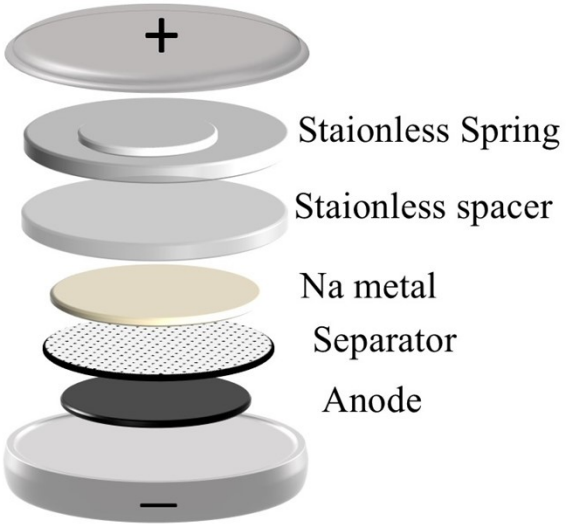

Fig. S5. Model diagram for Na-ion battery assembly.

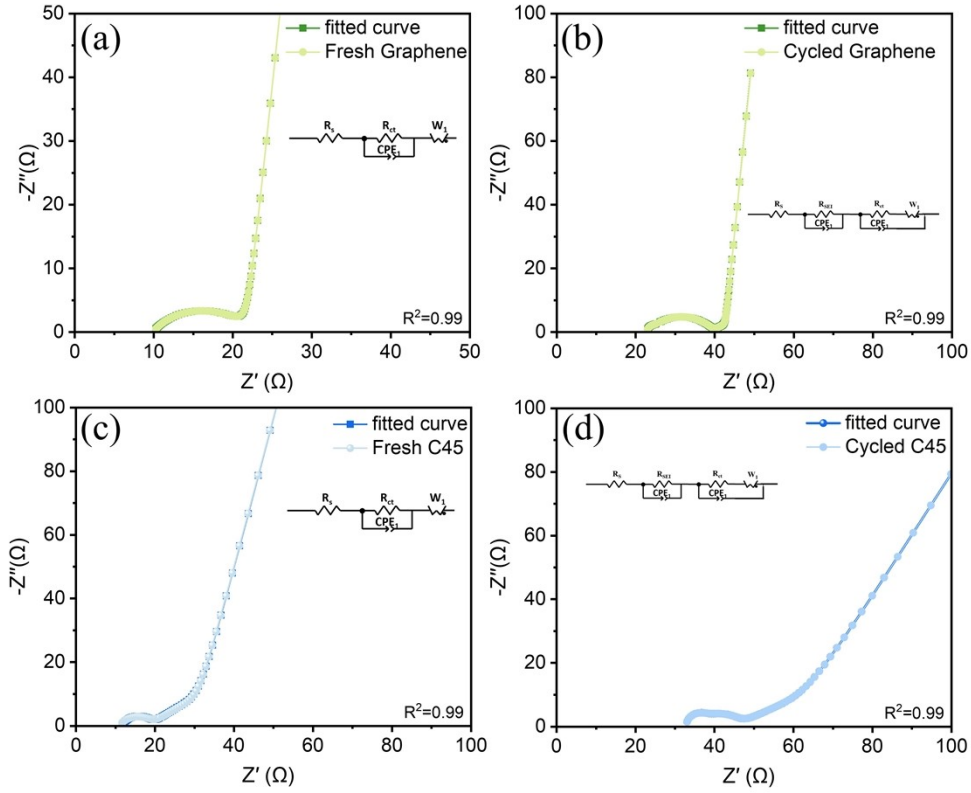

Fig. S6. Fit quality of (a) fresh graphene, (b) cycled graphene, (c) fresh C45, and (d) cycled C45.

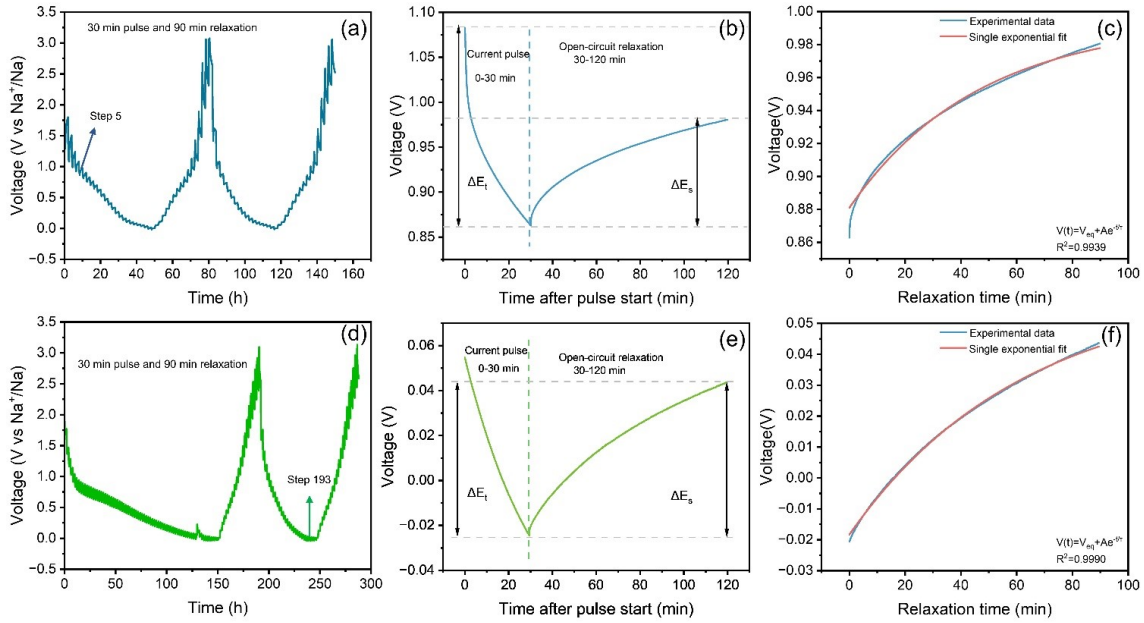

Fig. S7. (a–c) C45 electrode and (d–f) graphene electrode. (a, d) full GITT voltage–time profile, (b,e) enlarged view of the representative pulse with a 30 min current pulse and a 90 min relaxation period, and (c, f) single-exponential fitting of the relaxation region.

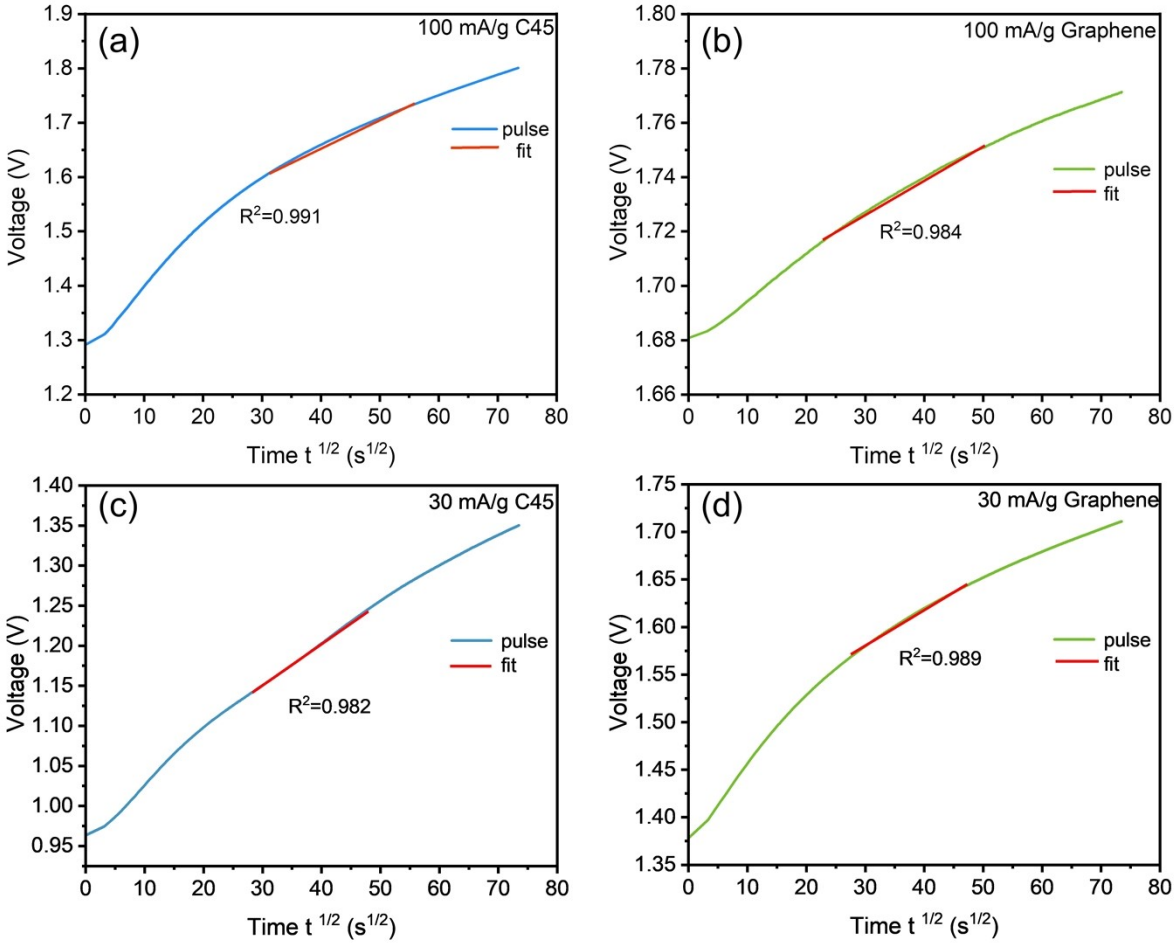

Fig. S8. Voltage as a function of the square root of time for a single charging current pulse duration with the corresponding linear fit for C45 and graphene at current densities of (a, b) 100 and (c, d) 30 mA g^{-1}.

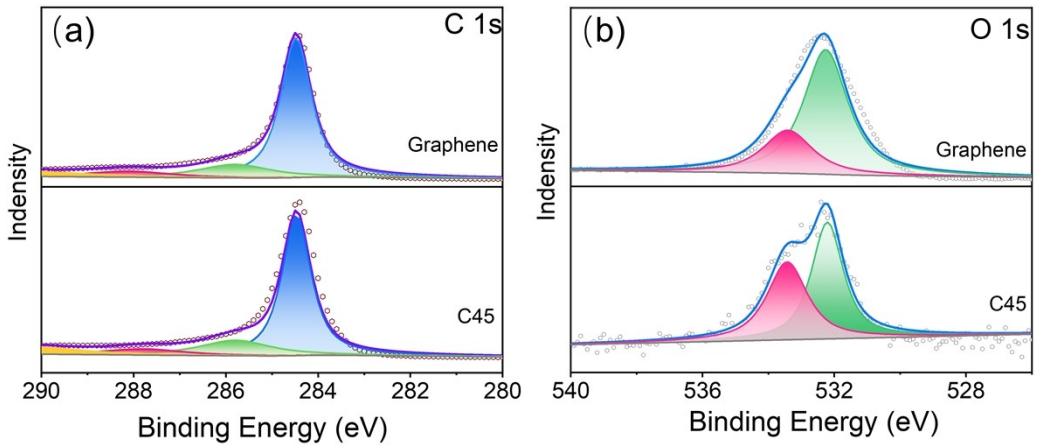

Fig. S9. (a) C1s and (b) O1s X-ray photoelectron spectra of graphene and C45.

Supplementary Tables

Table S1. Comparison of the D_{Na^+} values measured for the cathodic and anodic peaks observed in the CV curves of C45 and graphene with selected samples reported in the literature.

Material	Cathodic Na^+ diffusion	Anodic Na^+ diffusion	Reference
Hard carbon	4.9×10^{-9} cm^2 s^{-1}	3.5×10^{-9} cm^2 s^{-1}	[25]
Al–MoS^2@rGO	1.60×10^{-10} cm^2 s^{-1}	0.91×10^{-10} cm^2 s^{-1}	[26]
Sulfur-doped carbon	1.48×10^{-9} cm^2 s^{-1}	6.09×10^{-9} cm^2 s^{-1}	[27]
C45	1.1×10^{-8} cm^2 s^{-1}	1.8×10^{-8} cm^2 s^{-1}	This work
Graphene	2.7×10^{-9} cm^2 s^{-1}	1.1×10^{-8} cm^2 s^{-1}	This work

Table S2. D_{Na^+} values measured for the discharge and charge cycles observed in the GITT curves of C45 and graphene and those reported in the literature.

Material	Discharge Na^+ diffusion (cm^2 s^{-1})	Charge Na^+ diffusion (cm^2 s^{-1})	Reference
SnS_x@C	1.36×10^{-9}	3.49×10^{-11}	[47]
MoO_2@HCNFs	8.74×10^{-12} to 1.37×10^{-12}	3.09×10^{-11} to 1.87×10^{-13}	[48]
PET-derived hard carbon	6×10^{-11}	1×10^{-10}	[49]
C45 (30 mA g^{-1})	7.74×10^{-10} (1st) 1.3×10^{-9} (2nd)	1.6×10^{-9} (1st) 1.43×10^{-9} (2nd)	This work
C45 (100 mA g^{-1})	2.4×10^{-10} (1st) 3.8×10^{-10} (2nd)	3.8×10^{-10} (1st) 3.9×10^{-10} (2nd)	This work
Graphene (30 mA g^{-1})	1.77×10^{-10} (1st) 5.4×10^{-10} (2nd)	5.27×10^{-10} (1st) 5.10×10^{-9} (2nd)	This work
Graphene (100 mA g^{-1})	9.18×10^{-10} (1st) 2.02×10^{-9} (2nd)	3.0×10^{-9} (1st) 3.0×10^{-9} (2nd)	This work

Table S3. D_{Na^+} values measured using electrochemical impedance spectroscopy (EIS) curves of C45 and graphene and those reported in the literature.

Material	Na^+ diffusion	Reference
RP@Ni-P	1.04×10^{-14}	[65]
VPO_4@C	2.35×10^{-14}	[66]
Nb-doped TiO_2	4.31×10^{-13}	[67]
C45	4.75×10^{-14} (Fresh) 5.30×10^{-13} (cycled)	This work
Graphene	4.99×10^{-14} (Fresh) 8.40×10^{-11} (cycled)	This work

Table S4. Structural and surface properties of the nanocarbon materials, including specific

surface area (SSA), average pore diameter (APD), electrical conductivity (EC), and pore volume (PV).

Parameter	Graphene	C45
(002) peak position (°)	26.3	25.1
d_{002} (nm)	0.34	0.35
Crystalline size (nm)	28.1	1.6
Raman I_D/I_G	1.09	1.32
SSA ($m^2\ g^{-1}$)	242.5	60.8
APD (nm)	17.4	13.2
EC ($S\ m^{-1}$)	1336	640
PV ($cm^3\ g^{-1}$)	0.82	0.15
Conductivity ($S\ m^{-1}$)	1335	640

Table S5. Values of various resistances measured for fresh and cycled cells made of C45 and graphene electrodes, extracted from Figs. 3 and 4.

Carbon	State	R_s (Ω)	R_{ct} (Ω)	R_{SEI} (Ω)
C45	Fresh	15.9	11.9	-
	Cycled	33.1	16.0	11.3
Graphene	Fresh	11.6	6.8	-
	Cycled	22.5	0.7	16.3

Table S6. Parameters used in the equation for the CV method.

Scan rate (mV/s)	$V^{1/2}\cdot S^{1/2}$	C45 cathodic peak current (A)	C45 Anodic peak current (A)	Graphene cathodic peak current (A)	Graphene Anodic peak current (A)	Electrode area, A (cm^2)	Concentration, C_0 ($mol\ L^{-1}$)	Electron number
0.2	0.01414	−0.371	0.411	−0.227	0.0745	1.1304	1	1
0.4	0.02	−0.645	0.559	−0.395	0.147	1.1304	1	1
0.6	0.02449	−0.828	0.702	−0.535	0.216	1.1304	1	1
0.8	0.02828	−0.978	0.822	−0.666	0.285	1.1304	1	1
1.0	0.03162	−1.08	0.896	−0.78	0.35	1.1304	1	1

Table S7. Parameters used in the EIS measurements.

Material	Gas constant (R) (J mol^{-1})	Electrode surface area (A)(cm^2)	Na^+ concentration (C) (mol L^{-1})	Number of electrons (n)	Faraday Constant (F) (C mol^{-1})	Warburg Coefficient (σ) (Ω $s^{-11/2}$)
Fresh C45	8.314	1.13	0.010647	1	96485	70.59
Fresh Graphene	8.314	1.13	0.010647	1	96485	68.91
Cycled C45	8.314	1.13	0.010647	1	96485	21.1
Cycled Graphene	8.314	1.13	0.010647	1	96485	1.68

Reference

1. X. Yang and A. L. Rogach, Adv. Energy Mater., 2019, 9, 1900747.
2. Y. X. Qin, Z. T. Pan, X. X. Liu, H. P. Lu, L. Xian and L. B. Kong, J. Mater. Chem. A, 2026, 14, 12394–12403
3. M. Rafiee, D. J. Abrams, L. Cardinale, Z. Goss, A. Romero-Arenas and S. S. Stahl, Chem. Soc. Rev., 2024, 53, 566–585.
4. R. Dugas, J. D. Forero-Saboya and A. Ponrouch, Chem. Mater., 2019, 31, 8613–8628.
5. Y. Gao, Z. Lv, S. Zhang, K. Hu, T. Lin and F. Huang, Nano Lett., 2026, 26, 3524–3532.
6. D. M. de Rooij, Anti-Corros. Methods Mater., 2003, 50, 276–281.
7. G. Ryoo, J. Shin, B. G. Kim, D. G. Lee, J. T. Han, B. Park, et al., Chem. Eng. J., 2024, 496, 154081.
8. N. Elgrishi, K. J. Rountree, B. D. McCarthy, E. S. Rountree, T. T. Eisenhart and J. L. Dempsey, J. Chem. Educ., 2018, 95, 197–206.
9. M. G. Trachioti, A. C. Lazanas and M. I. Prodromidis, Microchim. Acta, 2023, 190, 251.
10. R. S. Nicholson, Anal. Chem., 1965, 37, 1351–1355.
11. K. Ngamchuea, S. Eloul, K. Tschulik and R. G. Compton, J. Solid State Electrochem., 2014, 18, 3251–3257.
12. A. L. Eckermann, D. J. Feld, J. A. Shaw and T. J. Meade, Coord. Chem. Rev., 2010, 254,

1769–1802.

13. H. M. Amin, Y. Uchida, C. Batchelor-McAuley, E. Kätelhön and R. G. Compton, J. Electroanal. Chem., 2018, 815, 24–29.
14. Z. Liu, J. Huang, B. Liu, D. Fang, T. Wang, Q. Yang, L. Dong, G. H. Hu and C. Xiong, Energy Storage Mater., 2020, 24, 138–146.
15. B. Deka Boruah, A. Mathieson, S. K. Park, X. Zhang, B. Wen, L. Tan, A. Boies and M. De Volder, Adv. Energy Mater., 2021, 11, 2100115.
16. D. Commandeur, V. Stolojan, M. Felipe-Sotelo, J. Wright, D. Watson and R. C. T. Slade, J. Mater. Chem. A, 2025, 13, 34493–34506.
17. A. S. Vedpathak, S. A. Sahu, T. N. Shinde, S. S. Kalyane, S. S. Warule, R. S. Kalubarme, et al., J. Mater. Chem. A, 2025, 13, 10736–10748.
18. Y. Zhang, J. Huang, L. Qiu, R. Jiao, Y. Zhang, G. Yang, et al., ACS Appl. Mater. Interfaces, 2024, 16, 27684–27693.
19. G. Ryoo, M. J. Kim, M. S. Kim, S. Shin, J. W. Lee, B. G. Kim, et al., Small Methods, 2025, 9, 2401801.
20. S. A. Odom, S. Ergun, P. P. Poudel and S. R. Parkin, Energy Environ. Sci., 2014, 7, 760–767.
21. Y. Zhang, Y. Huang, V. Srot, P. A. van Aken, J. Maier and Y. Yu, Nano-Micro Lett., 2020, 12, 165.
22. C. Punckt, M. A. Pope and I. A. Aksay, J. Phys. Chem. C, 2013, 117, 16076–16086.
23. F. Wu, Y. Li, M. Wang, W. He, M. Jiang, D. Su, et al., J. Mater. Chem. A, 2026, DOI: 10.1039/D6TA02428A.
24. Z. Long, H. Jia, R. Zhang, W. Li, K. Wang and H. Qiao, J. Mater. Chem. A, 2026, DOI: 10.1039/D6TA01272H.
25. G. Maresca, A. Petrongari, S. Brutti and G. B. Appetecchi, ChemSusChem, 2023, 16, e202300840.
26. M. K. Singh, J. Pati, D. Seth, J. Prasad, M. Agarwal, M. A. Haider, J.-K. Chang and R. S. Dhaka, Chem. Eng. J., 2023, 454, 140140.
27. T. Neff, J. Heßdörfer, A. Bilican, L. Kolb, F. Reinert and A. Krueger, Electrochim. Acta, 2025, 537, 146912.

28. S. D. Kang and W. C. Chueh, J. Electrochem. Soc., 2021, 168, 120504.
29. D. W. Dees, S. Kawauchi, D. P. Abraham and J. Prakash, J. Power Sources, 2009, 189, 263–268.
30. J. S. Horner, G. Whang, D. S. Ashby, I. V. Kolesnichenko, T. N. Lambert, B. S. Dunn, A. A. Talin and S. A. Roberts, ACS Appl. Energy Mater., 2021, 4, 11460–11469.
31. J. H. Park, H. Yoon, Y. Cho and C. Y. Yoo, Materials, 2021, 14, 4683.
32. C. Deng and W. Lu, J. Power Sources, 2020, 473, 228613.
33. K. Chayambuka, G. Mulder, D. L. Danilov and P. H. L. Notten, J. Power Sources Adv., 2021, 9, 100056.
34. Y. C. Chien, H. Liu, A. S. Menon, W. R. Brant, D. Brandell and M. J. Lacey, Nat. Commun., 2023, 14, 2289.
35. Y. Zhu and C. Wang, J. Phys. Chem. C, 2010, 114, 2830–2841.
36. T. Xu, Z. Yao, W. Jiang, Y. Chen, C. Liu, Y. Guan, et al., J. Mater. Chem. A, 2025, 13, 29471–29485.
37. W. Xie, Z. Zhang and X. Gao, Electrochim. Acta, 2024, 493, 144396.
38. E. Talaie, P. Bonnick, X. Sun, Q. Pang, X. Liang and L. F. Nazar, Chem. Mater., 2017, 29, 90–105.
39. T. Schied, A. Nickol, C. Heubner, M. Schneider, A. Michaelis, M. Bobeth and G. Cuniberti, ChemPhysChem, 2021, 22, 885–893.
40. M. Jia, W. Zhang, X. Cai, X. Zhan, L. Hou, C. Yuan and Z. Guo, J. Power Sources, 2022, 543, 231843.
41. X. H. Rui, N. Ding, J. Liu, C. Li and C. H. Chen, Electrochim. Acta, 2010, 55, 2384–2390.
42. M. E. Houck, A. S. Groombridge, M. F. De Volder and A. M. Boies, Cell Rep. Phys. Sci., 2023, 4, 101410.
43. J. Kim, S. Park, S. Hwang and W. S. Yoon, J. Electrochem. Sci. Technol., 2022, 13, 19–31.
44. C. H. Chen, F. Brosa Planella, K. O'Regan, D. Gastol, W. D. Widanage and E. Kendrick, J. Electrochem. Soc., 2020, 167, 080534.
45. A. Verma, K. Smith, S. Santhanagopalan, D. Abraham, K. P. Yao and P. P. Mukherjee, J. Electrochem. Soc., 2017, 164, A3380–A3392.

46. Y. Zhang, Q. Fu, Q. Xu, X. Yan, R. Zhang, Z. Guo and G. Chen, Nanoscale, 2015, 7, 12215–12224.
47. A. P. Nowak, P. Rutecki, M. Szkoda and K. Trzciński, Energies, 2024, 17, 3233.
48. N. Feng, M. Gao, J. Zhong, C. Gu, Y. Zhang and B. Liu, Polymers, 2024, 16, 1452.
49. C. Wang, M. Luo, S. Song, M. Tang, X. Wang and H. Liu, Materials, 2025, 18, 1166.
50. B. Y. Chang and S. M. Park, Annu. Rev. Anal. Chem., 2010, 3, 207–229.
51. J. Kaspar, M. Graczyk-Zajac and R. Riedel, Electrochim. Acta, 2014, 115, 665–670.
52. E. P. Randviir and C. E. Banks, Anal. Methods, 2013, 5, 1098–1115.
53. Y. Fernández-Pulido, I. Cameán, B. Lobato and A. B. García, J. Energy Storage, 2026, 155, 121427.
54. A. Piccardi, S. Pettinato, M. C. Rossi, M. Girolami and S. Salvatori, Electronics, 2025, 14, 4048.
55. W. Li, J. Cui, W. Ye, P. Su, X. Song, T. Yang and Z. Chen, J. Mater. Chem. A, 2025, 13, 18388–18397.
56. L. A. Middlemiss, A. J. Rennie, R. Sayers and A. R. West, J. Electrochem. Soc., 2024, 171, 010528.
57. J. Bisquert and A. Compte, J. Electroanal. Chem., 2001, 499, 112–120.
58. J. Huang, Electrochim. Acta, 2018, 281, 170–188.
59. D. Ledwoch, L. Komsiyska, E. M. Hammer, K. Smith, P. R. Shearing, D. J. L. Brett and E. Kendrick, Electrochim. Acta, 2022, 401, 139481.
60. M. Gaberšček, Curr. Opin. Electrochem., 2022, 32, 100917.
61. M. Gaberšček, Nat. Commun., 2021, 12, 6513.
62. P. Wang, S. Xu, S. Wang, T. Xia, J. Bai, X. Zhu, Y. Sun, Y. Li, X. Wu, X. He and B. Zhao, ACS Nano, 2025, 19, 38735–38748.
63. M. Janssen and J. Bisquert, J. Phys. Chem. C, 2021, 125, 15737–15741.
64. S. C. Adediwura, N. Mathew and J. S. auf der Günne, J. Mater. Chem. A, 2024, 12, 15847–15857.
65. S. Liu, J. Feng, X. Bian, J. Liu, H. Xu and Y. An, Energy Environ. Sci., 2017, 10, 1222–1233.
66. X. H. Rui, N. Yesibolati, S. R. Li, C. C. Yuan and C. H. Chen, Solid State Ionics, 2011,

187, 58–63.

67. F. Zhao, B. Wang, Y. Tang, H. Ge, Z. Huang and H. K. Liu, J. Mater. Chem. A, 2015, 3, 22969–22974.

68. A. R. Kamali, Green Production of Carbon Nanomaterials in Molten Salts and Applications, Springer, Singapore, 2020.